HT-FED04-56251

Computational Model for Predicting the Location of Glass Solidification in Optic Fiber Drawing

Zhiyong Wei* and Kok-Meng Lee
The George W. Woodruff School of Mechanical Engineering
Georgia Institute of Technology,
Atlanta, GA 30332-0405
gte384w@mail.gatech.edu, kokmeng.lee@me.gatech.edu
*Tel: (404)894-2642; Fax: (404)894-9342

Zhi Zhou and Siu-Ping Hong
OFS
Norcross, GA 30071
Email: zhizhou@ofsoptics.com, siupinghong@yahoo.com

ABSTRACT

This paper presents a computational model for predicting the location at which the glass fiber solidifies during a high-speed drawing process. Although modeling of the optic fiber drawing process has been of interest for the past two decades, traditional fiber drawing process uses small diameter preforms and low draw speeds, where the glass usually solidifies and turns into fiber inside the furnace. Much larger preforms drawn at higher speeds have been used in the state-of-the-art fiber drawing systems to improve production efficiency and reduce cost. Insulated post-chambers are often added below the furnace to reduce the glass cooling rate so that the optical loss in the fiber is low. To provide a basis for design optimization of the post-chamber, we have solved the conjugate problem of the glass free surface flow and the air convection to determine the location where the glass solidifies. As radiation is the dominant mode of heat transfer in the glass, the radiative transfer equation (RTE) is solved directly by discrete ordinate method (DOM). The heat flux due to the mixed convection of the air is also numerically calculated along the glass free surface, which involves the boundary layer flow around a continuously moving fiber and the buoyancy driven flow through the open-ended channel. The calculated free shapes are compared against the experimentally measured data to verify the computational model.

Keywords: optic fiber drawing, computational, solidification

1. INTRODUCTION

To meet the growing demands of optic fibers in (the long haul and the last-mile access) networking applications, fiber manufacturers are seeking methods to draw fibers at high speeds from large preforms (glass rods) in order to improve production efficiency, fiber quality, and save manufacturing cost.

Figure 1 shows a typical modern fiber-drawing process. The preform is moved slowly into a cylindrical furnace and heated above its melting temperature (about 1580ºC for fused silica). The preform becomes soft and melts to form a neck-down profile inside the furnace. The glass cools slowly in the insulated post-chamber during its gradual solidification before leaving the iris (a small opening) at the bottom of the post-chamber; the slow cooling is essential to reduce optical losses in the final product so that the quality specifications can be met. Driven by buoyancy force, the ambient air may enter the chamber through the iris and exit the furnace at the top ring opening. The speed of the glass flow in most part of the post-chamber increases drastically (as high as 50 times) from the glass speed at the furnace exit. A boundary layer of air starts to develop along the continuously moving glass cylinder. Our interest is to predict the location of the fiber solidification and the corresponding temperature gradient of the glass fiber for the optimal design of the drawing process and the post-chamber. This requires solving the conjugate problem of the temperature coupled glass free surface flow and the mixed convection of the air inside the open-ended chamber.
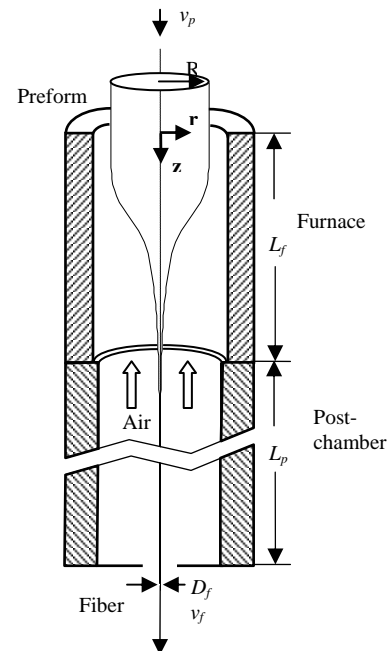

Figure 1 Schematic of fiber drawing process

Modeling of the high-speed fiber-drawing process with large-diameter performs is challenging in that the free surface flow is strongly coupled with the radiative transfer in the glass and the air convection at the glass surface. During the late 1970's and the 1980's, various aspects of the optical fiber draw problems were studied by a number of researchers, which

include Paek and Runk [1], Homsy and Walker [2], Myers [3], and Vasiljev et al [4]. These studies primarily based on 1D model. Two-dimensional (2D) models have been developed in more recent studies. Based on the radially lumped axial velocity and the axial force balance, Choudhury et al. [5] obtained a correction scheme to generate the neck-down profile while solving the 2D energy and momentum equations. Xiao and Kaminski [6] solved the 2D conjugate problem using the commercial finite element code FIDAP. They studied a 5cm diameter preform and it was shown that the glass velocity distribution is close to 1D while the glass temperature has a 2D distribution. Other 2D studies include Lee and Jaluria [7], Choudhury and Jaluria [8], Yin and Jaluria [9] and Cheng and Jaluria [10]. The above studies only considered the furnace domain, and have based on either one of the two assumptions; the fiber solidifies within the furnace, or an arbitrary glass diameter is specified at the furnace exit. These assumptions are only valid for drawing small diameter preforms at a low speed.

The gas flow in the conjugate transport during the fiber drawing process has been numerically solved by a number of researchers (Choudhury et al. [11], Choudhury and Jaluria [12], Xiao and Kaminski [6]), where both aiding and opposing (laminar and incompressible) gas flows with a given flow rate were considered. However, the effects of the buoyancy driven open-ended channel flow (along with temperature-dependent physical properties) have not been considered in [6] [11] [12]. In modern drawing processes (Figure 1), the air boundary layer flow developed along the continuously moving fiber may turn into turbulent in a long post-chamber, where the effects of turbulence on the fiber cooling should be investigated.

In order to predict the location of the glass solidification in modern fiber drawing processes, where large diameter preforms and high draw speeds are used, we consider here *both the furnace and the post-chamber* in solving the conjugate problem of the temperature coupled free surface glass flow and the mixed convection of the air. Due to large temperature variations, we account for the temperature dependency of the air properties. Unlike previous studies [1][5] where comparisons were made against experimental data obtained for a small-diameter preform (1 cm) drawn at a slow speed (1 m/s), we compare our prediction against experimentally measured neck-down profile drawn at 18 m/s. The post-chamber wall temperature and fiber temperature were also measured for verifying the calculation. The model presented here can be applied to the design optimization of a high-speed draw process.

2. ANALYSIS

The following assumptions are made in the formulation:

1. The glass flow is Newtonian and incompressible.

2. The surface tension at the glass free surface is neglected since it is several orders of magnitude smaller than the viscous force.

3. The glass is semitransparent to radiation in the range $0<\lambda<5\mu$m and is almost opaque beyond $5\mu m$. The scattering of radiation can be neglected (Viskanta, [13]). Based on the fact that the surface of the melting preform may undergo wavy hydrodynamic instabilities with the magnitude in the order of radiation wavelengths, the inner and outer surfaces at the glass/air interface are treated as diffuse for the radiation reflection and transmission.

4. Previous 2D computations in the furnace domain [5] [6] [10] have shown that the flow in the neck-down region is close to 1D for preforms up to 5cm in diameter, while the temperature distribution is 2D. As a first attempt to predict the fiber solidification, we use a 1D glass flow model with a 2D thermal model. The radially lumped temperature is used to obtain the glass viscosity. This semi-2D model for the glass greatly reduces the computational cost.

2.1 2D Heat Transfer Model

The highly viscous glass flow is strongly coupled with the heat transfer through the temperature-dependent viscosity. We solve two axisymmetric thermal transport problems for the glass temperature: the radiation transfer in the semitransparent glass and the mixed convection of the air in the open-ended chamber.

Glass domain

The glass energy equation is given by

$$\rho C_p \left(\frac{\partial T}{\partial t} + \mathbf{v} \cdot \nabla T \right) = -\nabla \cdot \left(-k\nabla T + \mathbf{q}_R \right) + \mu \Phi \tag{1}$$

where $\mathbf{v}$ is the velocity vector; T is the temperature; ρ, C_p, k, μ are the density, the specific heat, the thermal conductivity and the viscosity, respectively; $\mathbf{q}_R$ is the radiative heat flux in the glass domain; and Φ is the viscous dissipation function. The boundary conditions for the energy equation are given by

at $r = 0$
$$\frac{\partial T}{\partial r} = 0 \tag{2}$$

at $z = 0$ and L
$$\frac{\partial^2 T}{\partial z^2} = 0 \tag{3}$$

at $z = R(z)$
$$-k\mathbf{n} \cdot \nabla T = q_{rad,opa} + q_{conv} \tag{4}$$

where $\mathbf{n}$ is the unit normal along the free surface; $q_{rad,opa}$ is the net radiation heat flux in the opaque band; and q_{conv} is the convective heat flux from the air.

Radiation is the dominant mode of heat transfer in the neck-down region. The divergence of $\mathbf{q}_R$ can be obtained by

$$\nabla \cdot \mathbf{q}_R = \int_0^\infty \left[4\pi\kappa_\lambda n_\lambda^2 I_{b\lambda}(T) - \kappa_\lambda \int_{\Omega=4\pi} I_\lambda(\mathbf{r},\mathbf{s}) d\Omega \right] d\lambda \tag{5}$$

where the spectral radiation intensity $I_\lambda(\mathbf{r},\mathbf{s})$ is a function of the position vector $\mathbf{r}$, orientation vector $\mathbf{s}$, and wavelength λ; $I_{b\lambda}(T)$ is the spectral blackbody radiation intensity given by Planck's function; Ω is the solid angle; κ_λ is the spectral absorption coefficient; and n_λ is the spectral index of refraction. The radiation intensity is obtained by solving the radiative transfer equation (RTE):

$$\mathbf{s} \cdot \nabla I_\lambda(\mathbf{r},\mathbf{s}) = \kappa_\lambda \left[n_\lambda^2 I_{b\lambda}(T) - I_\lambda(\mathbf{r},\mathbf{s}) \right] \tag{6}$$

In this study, the discrete ordinate method (DOM) is used to solve the RTE which is transformed in a fully conservative form in a general curvilinear coordinate system. An enclosure analysis for the radiation exchange among the glass outer surface, the furnace wall and the top and the bottom disk openings is carried out to obtain the irradiations on the free surface. These calculated irradiations are used to obtain $q_{rad,opa}$ and the boundary radiation intensities for the glass domain. A detailed procedure of the method along with the boundary conditions and the fused silica radiation properties can be found in Wei et al.

[14] except that the intensities from the outside of the chamber at the top and bottom of the glass domain are neglected.

Air domain

The glass temperature boundary condition along the free surface requires the solution of q_{conv}, which is significant in the post-chamber due to the high surface area to volume ratio and the high moving speed of the glass. We obtain q_{conv} by numerically solving the following 2D continuity, momentum and energy equations for the air temperature field of the mixed convection in the furnace and post-chamber.

$$\frac{\partial \rho}{\partial t} + \nabla \cdot (\rho \mathbf{v}) = 0 \tag{7}$$

$$\rho\left(\frac{\partial v}{\partial t} + \mathbf{v} \cdot \nabla \mathbf{v}\right) = -\nabla p + \nabla \cdot \left[(\mu + \mu_T)(\nabla \mathbf{v} + \nabla \mathbf{v}^T)\right] + \rho \mathbf{g} \tag{8}$$

$$\rho C_p\left(\frac{\partial T}{\partial t} + \mathbf{v} \cdot \nabla T\right) = -\nabla \cdot \left[-(k + k_T)\nabla T\right] \tag{9}$$

where p is the pressure; $\mathbf{g}$ is the gravity acceleration vector; and μ_T and k_T are the turbulent viscosity and conductivity.

The algebraic mixing-length turbulence model with the empirical correlation of eddy viscosity is used to obtain μ_T in Equation (8). The classical van Driest damping function (van Driest [15]) is used for the "law-of-the-wall" inner region, while for the "wake-like" log-law zone, the following correlation of eddy viscosity (Lueptow and Leehey, [16]) is used:

$$\mu_T = c\rho\delta U_\tau \tag{10}$$

where c is an empirical constant and δ is the local boundary layer thickness. The friction velocity U_τ is calculated using a momentum integral relation for an axisymmetric boundary layer presented by Lueptow, et al. [17]. The eddy conductivity k_T is then obtained using μ_T and the unit turbulent *Prandtl* number.

The boundary conditions for the air domain are given by

at $z = 0$ $\quad \frac{\partial u}{\partial z} = \frac{\partial v}{\partial z} = \frac{\partial T}{\partial z} = 0, \; p = p_\infty$ $\tag{11}$

at $r = R(z)$ $\quad u = u_g, \; v = v_g, \; T = T_g$ $\tag{12}$

at $r = R_{fur}$ $\quad u = v = 0, \; T = \begin{cases} T_{fur} & z < L_f \\ T_{po} & z > L_f \end{cases}$ $\tag{13}$

at $z = L$
and $r < R_{ope}$ $\quad \frac{\partial u}{\partial z} = \frac{\partial v}{\partial z} = 0, \; \begin{cases} \partial T/\partial z = 0 & (v > 0) \\ T = T_{amb} & (v < 0) \end{cases}$ $\tag{14}$

$$p - p_\infty = -\frac{1}{2}\rho\bar{v}^2, \; \bar{v} = \frac{2}{R_{ope}^2 - R_f^2}\int_{R_f}^{R_{ope}} vr\,dr$$

at $z = L$
and $r > R_{ope}$ $\quad u = v = 0, \; T = T_{iris}$ $\tag{15}$

where R_{fur}, R_{ope} and R_f are the radii of the furnace, the iris opening, and the fiber, respectively; p_∞ is the ambient pressure; T_{fur} and T_{po} are the furnace temperature and the post-chamber temperature, respectively; T_{amb} is the ambient temperature; and T_{iris} is the iris temperature. No-slip boundary condition has been used along the channel surfaces. The Bernoulli Equation is used to obtain the pressure at the inlet cells at the iris opening.

The governing equations for the air domain are first transformed into the curvilinear coordinate system, and then discretized on a staggered grid. A 2nd order upwind scheme is used to discretize the convective term. The Navier-Stokes equations are solved using the time marching scheme and the Pressure-Implicit with Splitting of Operators (PISO) algorithm (Issa, [18]).

2.2 1D Glass Flow Model

The 1D steady state glass flow model for the free surface fiber drawing process can be derived using the mass conservation and vertical force balance as follows:

$$\frac{d}{dz}(v\pi R^2) = 0 \tag{16}$$

$$\rho\frac{d}{dz}(\pi R^2 v^2) = \frac{d}{dz}(\sigma_{zz}\pi R^2) + \rho g\pi R^2 \tag{17}$$

where v is the axial velocity; R is the glass radius which is a function of z; σ_{zz} is the axial normal stress; and g is the gravity acceleration. For a Newtonian fluid, the normal stress is given by

$$\sigma_{zz} = -p + 2\mu\frac{dv}{dz} \tag{18}$$

The pressure can be obtained from the normal force balance condition at the free interface:

$$p - p_a = 2\mu\mathbf{m}\cdot\nabla(\mathbf{n}\cdot\mathbf{v}) - 2\mu_a\mathbf{n}\cdot\nabla(\mathbf{n}\cdot\mathbf{v}_a) \tag{19}$$

where the subscript a denote the air side. Using Equation (16), (18) and (19) and the kinematic condition of the free surface, we have

$$\sigma_{zz} = 3\mu\frac{dv}{dz} \tag{20}$$

The detailed derivation of Equation (20) is given in the appendix. The above result is consistent with the elongational assumption made by Paek [1]. Although a similar free surface correction scheme has been suggested by Choudhury et al. [5], we revise the derivation which leads to a somewhat different solution.

The boundary conditions for $v(z)$ is given by

at $z = 0$ $\quad\quad\quad\quad\quad v = v_p$ $\tag{21a}$
at $z = L_f + L_p$ $\quad\quad\quad v = v_f$ $\tag{21b}$

where v_p is the preform feed rate; and v_f is the fiber drawing speed. Equation (21b) is only valid when the glass solidifies inside the post-chamber. If the glass temperature is above the melting point and the velocity continues to increase at the exit of the post-chamber, the post-chamber should be lengthened so that the glass solidifies inside the chamber to minimize optical losses.

From the mass conservation or Equation (16), we have the following relationship:

$$v = v_p\frac{R_p^2}{R^2} \tag{22}$$

where R_p is the preform radius. Substituting Equation (22) and (20) into the inertia and viscous terms respectively in Equation (17), and then integrating the resulting equation twice with respect to z, we yield the following expression for v:

$$v(z) = v_p - \int_0^z \frac{\rho g}{3\mu R^2}\left(\int_0^z R^2\,dz\right)dz$$
$$- \int_0^z \frac{1}{3\mu R^2}\left(\int_0^z \frac{2\rho R_p^4 v_p^2}{R^3}\,dR\right)dz + \int_0^z \frac{C_2}{3\mu R^2}\,dz + C_1 \tag{23}$$

3

where the integration constants are obtained by substituting the boundary conditions into the above equation:

$$C_1 = 0 \qquad (24a)$$

$$C_2 = \frac{1}{\int_0^L (\mu R^2)^{-1} dz} \left[v_f - v_p + \frac{\rho g}{3} \int_0^L \frac{1}{\mu R^2} \left(\int_0^z R^2 dz \right) dz \right.$$

$$\left. + \frac{\rho R_p^{\,4} v_p^{\,2}}{3} \int_0^L \frac{1}{\mu R^2} \left(\frac{1}{R_p^{\,2}} - \frac{1}{R^2} \right) dz \right] \qquad (24b)$$

where $L = L_f + L_p$. The results in Equation (23) and (24) are different from those derived by Choudhury et al. [5] which misses an expression in the denominator for C_2. An additional advantage in our derivation is the simpler expression for σ_{zz}. Given the axial velocity distribution $v(z)$, the glass free surface profile can be determined from Equation (22):

$$R(z) = \sqrt{\frac{v_p R_p^{\,2}}{v(z)}} \qquad (25)$$

Since the calculation of $v(z)$ in Equation (23) requires the information of $R(z)$, both v and R are solved iteratively.

3. STEADY STATE SIMULATION

A MATLAB program with C++ subroutines has been written to simulate the free surface of the draw process (Figure 1), where the furnace temperature was measured using a M90R single color infrared thermometer (MIKRON, Inc.). The preform radius is 0.045m and the furnace length is 0.45m; other values used in the simulation are listed in Table 1.

Table 1: Parameters used in the simulation

R_f (µm)	62.5	v_f (m/s)	18	$T_{fur,max}$ (K)	2400
R_{fur}/R_p	1.33	L_p/L_f	6.11	$T_{fur,min}$ (K)	1700
R_{post}/R_p	1.33				

The correlation obtained by Bansal [19] is used here to calculate the glass viscosity.

$$\mu(T) = 0.1 \exp(-14.368 + 61939.539/T) \qquad (26)$$

Other physical properties of the glass (fused silica) are taken from Fleming [20]. The empirical constant c in Equation (10) has been determined by Lueptow and Leehey [16] to be 0.0274.

During the furnace temperature measuring, the thermometer measures the radiation intensities of the furnace wall at the $0.65\mu m$ wavelength. Taking the multiple reflections in the furnace chamber into account, an enclosure analysis is carried out to obtain the emissive intensities and consequently, the temperature of the furnace wall. The temperature distribution is parabolic with the maximum at the middle and minimum at both ends. Since the thermometer cannot reach measure region beyond the furnace, the post-chamber temperature T_{po} is calculated by balancing the heat flux at the inner wall:

$$\varepsilon_p \left[E_{b,p}(T_{po}) - H_p \right] + k_a \left. \frac{\partial T_a}{\partial r} \right|_{r=R_{pi}} + \frac{T_{po} - T_{amb}}{R_{wall}} = 0 \qquad (27)$$

where ε_p, $E_{b,p}$ and H_p are the emissivity, block-body emissive power and irradiation at the post-chamber inner wall; R_{pi} is the post-chamber wall inner radius; and R_{wall} is the thermal resistance between T_{po} and T_{amb}, which can be obtained using the conductivity and thickness of the wall and the heat transfer coefficient at the outer wall.

Non-uniform grids were used so that grids near the free interface have a dense spacing; especially on the air side, the dimension of the first grid adjacent to the fiber surface is made at least less than half of the fiber radius (30µm) in order to account for the sharp gradients in the boundary layer. Based upon a grid size study, the grid numbers of 200×15 and 160×34 (in z and r directions, respectively) are used in the glass and the air domain, respectively.

3.1 Computation Algorithm

The steady-state free-surface of the glass, along with the velocity and temperature fields, has been solved as follows:

Step 1: Input the assumed initial free surface profile $R(z)$ and the values of the primitive variables $v(z)$ and $T(r, z)$.

Step 2: Conjugate temperature iteration (with a given free surface and the axial velocity distribution).
  a) The radial velocity component is given by $u = -0.5r(dv/dz)$ while satisfying the continuity equation.
  b) Calculate the view factors.
  c) Solve the mixed convection problem in the air domain for the heat flux along the free interface, $q_{conv} = -k_a (\mathbf{n} \cdot \nabla T)_a$.
  d) Solve the RTE, then calculate $\nabla \cdot \mathbf{q}_R$ using Equation (5).
  e) Solve Equation (1) using implicit time marching scheme.
  f) Repeat Step 2(d) until a steady state is reached.
  g) Repeat Step 2(c) until the glass temperature does not vary between two consecutive iterations.

Step 3: Free surface computation (with the temperature field obtained in Step 2).
  a) Calculate the glass viscosity using Equation (26) with the radially lumped temperature given by

$$\overline{T}(z) = \frac{2}{R_{fur}^{\,2} - R^2(z)} \int_{R(z)}^{R_{fur}} T(r, z) r \, dr .$$

  b) Calculate $v(z)$ using Equations (23) and (24).
  c) Update the free surface profile using Equation (25).
  d) Repeat Step 3(b) until the free surface profile does not change between two consecutive iterations.

Step 4: Regenerate the 2D curvilinear grid, and then repeat Step 2 until the relative change between two consecutive computed free surface profiles at Step 4 is less than 10-5.

The above procedures effectively reduce the variables to be solved during the computation by decoupling the temperature iteration and the free surface iteration. This results in a more robust and faster convergence in the computation.

3.2 Model Validation

In order to validate the numerical model, the steady-state free-surface profile of the glass rod was experimentally measured. In the experiment, the preform was taken out of the furnace in a short time (less than 1 minute) in order to prevent shape deformation due to the change in view factors. After the glass cooled down, the neck-down profile was measured by a laser scanner. Figure 2 compares the predicted free surface profile against the experimentally measured data drawn at 18m/s. As shown in the figure, the predicted free surface is in excellent agreement with the experimental measurement.

4

The post-chamber inner wall temperature was measured at several locations using thermo-couples, and compared against the calculated values in Figure 3, which are in good agreement. The fiber temperature at the exit of the post-chamber, which was measured by an infrared thermo camera, was around 1400K while the corresponding simulation result is 1418K. This close match (with less than 1.5% differences) validates the calculation of the mixed convection of the air around the fiber.
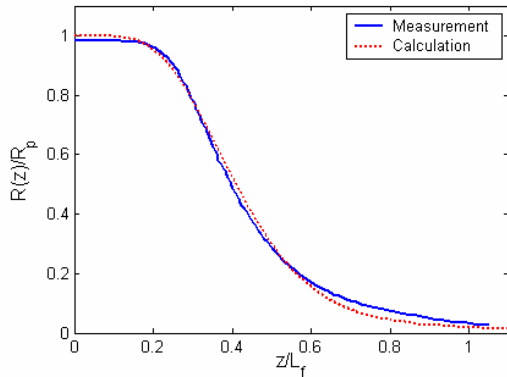

Figure 2 Model validations through free surface profiles

Figure 3 Post-chamber temperature validation

3.3 Simulation Results

For a given furnace/post-chamber configuration, an effective way to increase productivity is to draw the fiber at higher speeds. However, it is essential that the fiber solidifies before leaving the post-chamber. The effects of using higher draw speeds on the fiber at steady state were studied numerically using the values given in Table 1 for two draw speeds, v_f and $2v_f$. Some observations are briefly summarized as follows:

- The high draw speed has a tendency to increase the air convective flows; it is essential to account for the effects of the mixed air convection on the location of glass solidification in the design of a post-chamber. As shown in Figure 4, where the heat flux of the air convection and radiation along the glass free surface are computed, the air convection is negligible in the furnace but significant in the post-chamber as compared to the radiation.

- Figure 5(a) shows the predicted neck-down free surface profiles normalized to the preform radius. When the draw speed is increased, the neck-down profile is shifted or stretched downward to a certain extend. It is expected that the free surface region is longer for a higher draw speed.

- Figure 5(b) shows the axial glass temperature distributions normalized to the glass melting point (1580ºC). The

glass/fiber temperature decreases more slowly in the post-chamber under a higher draw speed. This implies that the effect of the advection increase on the glass temperature is much stronger than that of the air convection increase as the Reynolds number associated with the draw speed is higher.
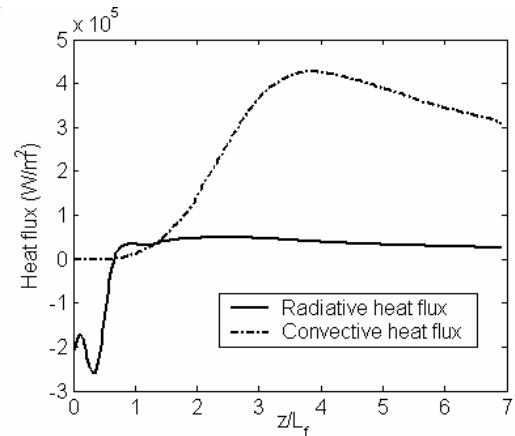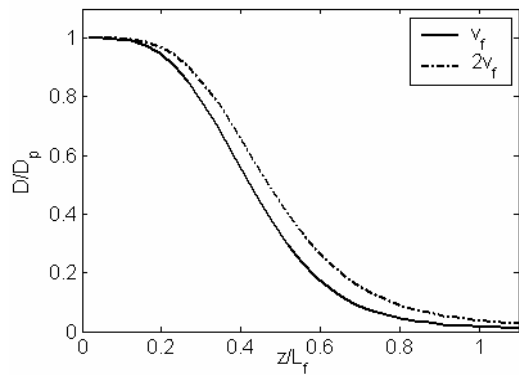

Figure 4 Heat fluxes along the free surface

- Figure 5(c) shows the convergence of the glass diameters to that of the fiber when the glass solidifies in the post-chamber. As shown in the figure, the fiber solidification is rather a gradual monotonically process than those of crystalline materials with a single phase transition temperature. Solid state glasses and fibers are actually non-crystalline super-cooled "liquid-like" melts. We define the location where the glass reaches within a bound of 0.25% about the steady state diameter (125µm) as the fiber solidification location.

- Figure 5(d) compares two methods of locating the fiber solidification for different draw speeds; namely, constant fiber diameter, and fiber melting temperature (1580ºC). The close match between the two methods shows that the glass viscosity at the melting point is high enough that the glass behaves like a solid. Hence, the glass (melting) temperature can be reasonably used to locate the fiber solidification.

Steady state solutions obtained for both speeds (as shown in Figure 5) imply that the fiber can be steadily drawn as configured. However, if the draw speed increases above $2.5v_f$, the fiber may solidify outside the post-chamber and thus, the trade-off for drawing at a higher speed than configured is that it requires a longer post-chamber.
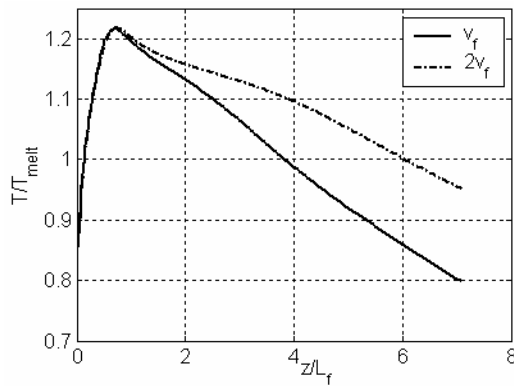
4. CONCLUSIONS

The computational model for predicting the location where the glass solidifies inside a post-chamber during a high-speed, continuous fiber drawing has been presented. Specifically, we have solved the conjugate problem of the glass temperature coupled with the mixed air convection around the fiber in both the furnace and post-chamber domains for the free surface geometry of the glass flow. The solution, which has been obtained by solving the 2D RTE directly using the DOM method and a steady-state free-surface updating scheme, has been validated by comparing the predicted free surface to an experimentally measured profile drawn at 18m/s. Our results show that the location of glass solidification determined by the glass diameter is consistent with that determined by locating the glass temperature equal to its melting temperature (1580ºC). The numerical model can be applied to the design optimization

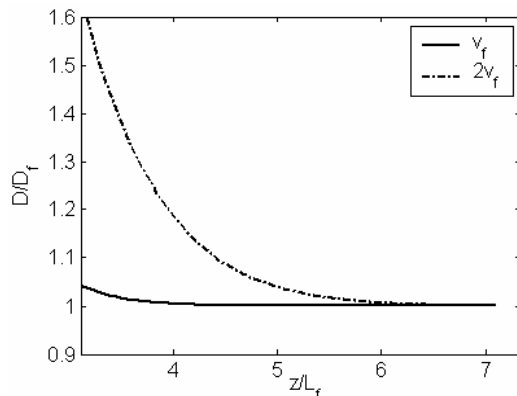5

Copyright © 2004 ASME

of the furnace/post-chamber configuration of a glass fiber drawing process.
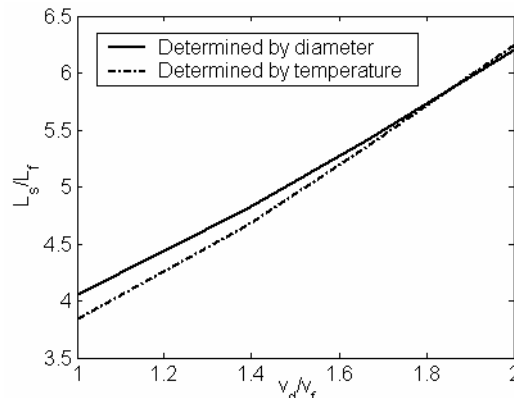

(a) Neck-down profiles

(b) Axial temperature distributions

(c) Fiber solidifications

(d) Fiber solidification locations
Figure 5 Effects of draw speed

REFERENCES

1. Paek, U. C., and R.B. Runk, 1978, "Physical Behavior of the Neck-Down Region during Furnace Drawing of Silica Fibers," *Journal of Applied Physics*, Vol. 49, pp. 4417-4422.
2. Homsy, G. M. and K. Walker, 1979, "Heat Transfer in Laser Drawing of Optical Fibers," Glass Techn., Vol. 20, No. 1, pp. 20-26.
3. Myers, M. R., 1989, "A Model for Unsteady Analysis of Preform Drawing," AIChE Journal, Vol. 35, No. 4, pp. 592-602.
4. Vasiljev, V.N., G.N. Dulnev, and V.D. Naumchic, 1989, "The Flow of a Highly Viscous Liquid with a Free Surface," Glass Technology, Vol. 30, No. 2, pp. 83-90.
5. Choudhury, S. R., Y. Jaluria, S. H.-K. Lee, 1999, "A Computational Method for Generating the Free-surface Neck-down Profile for Glass Flow in Optical Fiber Drawing," Numerical Heat Transfer, Part A, Vol. 35, pp. 1-24.
6. Xiao, Z. and D.A. Kaminski, 1997, "Flow, Heat Transfer, and Free Surface Shape During the Optical Fiber Drawing Process," HTD Vol. 347, National Heat Transfer Conf., ASME, Vol. 9, pp. 219-229.
7. Lee, S.H.-K. and Y. Jaluria, 1997, "Simulation of the Transport Processes in the Neck-Down Region of a Furnace Drawn Optical Fiber," Int. J. Heat Mass Transfer, Vol. 40, pp. 843-856.
8. Choudhury, S.R. and Y. Jaluria, 1998, "Thermal Transport Due to Material and Gas Flow in a Furnace for Drawing an Optical Fiber," J. Mater. Res., Vol. 13, No. 2, pp. 494-503.
9. Yin, Z. and Y. Jaluria, 2000, "Neck Down and Thermally Induced Defects in High-Speed Optical Fiber Drawing," ASME Journal of Heat Transfer, Vol. 122, pp. 351-362.
10. Cheng, X. and Y. Jaluria, 2002, "Effect of Draw Furnace Geometry on High-Speed Optical Fiber Manufacturing," Numerical Heat Transfer, Part A, Vol. 41, pp. 757-781.
11. Choudhury, S.R., Y. Jaluria, T. Vaskopulos, and C.E. Polymeropoulos, 1994 "Forced Convective Cooling of Optical Fiber During Drawing Process," J. of Heat Transfer, Vol. 116, pp. 790.
12. Choudhury, S.R. and Y. Jaluria, 1998, "Thermal Transport due to Material and Gas Flow in a Furnace for Drawing an Optical Fiber," J. Mater. Res., Vol. 13(2), pp. 494.
13. Viskanta, R., and E.E., Anderson, 1975, "Heat transfer in Semitransparent Solids," Advances in Heat Transfer, Vol. 11, pp.317-441.
14. Wei, Z. and K.M. Lee, S.W. Tchikanda, Z. Zhou, and S.P. Hong, 2003, "Effects of Radiative Transfer Modeling on Transient Temperature Distribution in Semitransparent Glass Rod," ASME Journal of Heat Transfer, Vol. 125, pp. 1-7.
15. Van Driest, E.R., 1956, "On Turbulent Flow Near a Wall," Journal of Aeronautical Science, Vol. 23, pp. 1007-1011.
16. Lueptow, R.M. and P. Leehey, 1986, "The Eddy Viscosity in a Turbulent Boundary Layer on a Cylinder," Physics of Fluids, Vol. 29(12), pp. 4232-4233.
17. Lueptow, R.M., P. Leehey, and T. Stellinger, 1985, "The Thick, Turbulent Boundary Layer on a Cylinder: Mean and Fluctuation Velocities," Physics of Fluids, Vol. 28(12), pp. 3495-3505.
18. Issa, R.I., 1985, "Solution of the Implicitly Discretized Fluid Flow Equations by Operator-Splitting," Journal of Computational Physics, Vol. 62, pp. 40-65.
19. Bansal, N.P. and R.H. Doremus, 1986, Handbook of Glass Properties, Academic Press, Inc., New York.
20. Fleming, J.D., 1964, "Fused Silica Manual," Final Report for the U.S. Atomic Energy Commission, Oak Ridge, Tennessee, Project No. B-153.

6

Copyright © 2004 ASME

APPENDIX

We derive here the elongation model given by Equation (20), which eliminates the pressure in Equation (18) using the free surface boundary condition given by Equation (19).

We began with the 1st term on the right-hand-side of Equation (19). The unit normal along the free surface pointing outward is given by

$$\mathbf{n} = n_r \hat{i} + n_z \hat{j} = \frac{1}{\sqrt{1+R'^2}}\hat{i} - \frac{R'}{\sqrt{1+R'^2}}\hat{j} \tag{A1}$$

where $\hat{i}$ and $\hat{j}$ are the unit vectors along the radial and axial directions respectively; and the prime denotes the derivative with respect to z. Using Equation (A1) and $\mathbf{v} = u\hat{i} + v\hat{j}$, it yields

$$\mathbf{n}\cdot\nabla(\mathbf{n}\cdot\mathbf{v}) = n_r^2\frac{\partial u}{\partial r} + n_r n_z\frac{\partial u}{\partial z} + n_z^2\frac{dv}{dz} + n_z\frac{dn_r}{dz}u + n_z\frac{dn_z}{dz}v \tag{A2}$$

where u and its partial derivatives are obtained as follows.

Along the free surface, we have the steady state kinematics:

$$u = vR' \tag{A3}$$

The derivative of Equation (A.3) with respect to z is given by

$$\frac{\partial u}{\partial z} = vR'' + \frac{dv}{dz}R' \tag{A4}$$

Using the 2D continuity equation $\partial u/\partial r + u/r + \partial v/\partial z = 0$ at the free surface and Equation (A3), we obtain

$$\frac{\partial u}{\partial r} = -\frac{vR'}{R} - \frac{dv}{dz} \tag{A5}$$

Substituting Equations (A1) and (A3)-(A5) into Equation (A2) and assuming R' is small (the maximum value of R' in our simulation is around 0.23, the square of which is 0.053<<1), we obtain the following equation upon simplification:

$$\mathbf{n}\cdot\nabla(\mathbf{n}\cdot\mathbf{v}) = \frac{1}{1+R'^2}\left(-\frac{R'}{R}v - \frac{dv}{dz}\right) \approx -\frac{R'}{R}v - \frac{dv}{dz} \tag{A6}$$

Expanding Equation (16) we obtain

$$\frac{R'}{R}v = -\frac{1}{2}\frac{dv}{dz} \tag{A7}$$

Thus, the 1st term in the right-hand-side of Equation (19) becomes

$$\mathbf{n}\cdot\nabla(\mathbf{n}\cdot\mathbf{v}) \approx -\frac{1}{2}\frac{dv}{dz} \tag{A8}$$

The pressure term in the 1D momentum equation for the solution of the velocity can be eliminated on the basis of the following arguments. Since the pressure variation on the air side can be neglected as compared to that on the glass side, the air pressure is taken as a reference and set to 0. Furthermore, the normal stress of the air is also negligible as compared to that of the glass. Hence, Equation (19) can be simplified to

$$p = 2\mu\mathbf{n}\cdot\nabla(\mathbf{n}\cdot\mathbf{v}) \tag{A9}$$

The pressure can be eliminated from Equation (18) by using Equation (A9) along with the substitution of Equation (A8).

NOMENCLATURE

C_p	Specific heat
$E_{b\lambda}$	Spectral blackbody emissive power
$E_{b,p}$	Blackbody emissive power on the post-chamber wall
H_p	Irradiation on post-chamber inner wall
I_λ	Spectral radiative intensity
$I_{b\lambda}$	Spectral blackbody intensity
L_f	Furnace length
L_p	Post-chamber length
L_s	Solidification location
R	Glass radius
R_f	Fiber radius
R_p	Preform radius
R_{pi}	Post-chamber wall inner radius
R_{ope}	Iris opening radius
R_{wall}	Thermal resistance of the post-chamber wall
T	Temperature
$\overline{T}$	Radially lumped temperature
T_{fur}	Furnace temperature
T_{po}	Post-chamber temperature
T_{amb}	Ambient temperature
U_z	Friction velocity
$\mathbf{v}$	Velocity vector
$\mathbf{g}$	Gravity acceleration vector
k	Thermal conductivity
n_λ	Index of refraction
$\mathbf{n}$	Unit normal vector
p	Pressure
$\mathbf{q}_R$	Radiation heat flux
$q_{rad,opa}$	Net radiation heat flux in the opaque band
q_{conv}	Convective heat flux from the air
r, z	Radial and axial coordinates
$\mathbf{r}$	Position vector
$\mathbf{s}$	Orientation vector
u, v	Radial and axial components of velocity
v_d, v_f	Draw speed, $v_f = 18$m/s
v_p	Preform feed rate
κ_λ	Spectral absorption coefficient
ε_p	Emissivity of the post-chamber wall
ρ	Density
μ	Dynamic viscosity
μ_T	Eddy viscosity
Φ	Dissipation function
σ_{zz}	Axial normal stress
Ω	Solid angle
δ	Boundary layer thickness
λ	Wavelength